Article:

Qian, B., Hu, J., Dutta, S. et al. (Accepted: 2026) Sensorless Displacement-Information-Recovery-Based Control for Piezoelectric Energy Harvesting With Adjustable Interfaces. IEEE Transactions on Industrial Electronics. ISSN: 0278-0046 (In Press)

Sensorless Displacement-Information-Recovery-Based Control for Piezoelectric Energy Harvesting With Adjustable Interfaces

Bo Qian, Jiahao Hu, Saikat Dutta, Weiqun Liu, *Member, IEEE*

***Abstract*—The existing studies on adjustable-parameter interfaces (APIs) have demonstrated their effectiveness in enhancing the output power and bandwidth of piezoelectric energy harvesters (PEHs). However, current self-sensing approaches remain constrained by information-poor signals or reliance on external sensors, restricting multi-parameter interface applicability. Moreover, under sensorless conditions, the mutual modulation between the piezoelectric response and adjustment behavior fundamentally impedes the realization of automation. To overcome the challenge, we propose a sensorless control scheme that interprets the electrical signal characteristics of piezoelectric elements in real time to provide instantaneous feedback for dynamic adjustment of interfaces. Specifically, a displacement information recovery module is designed to recover the displacement-related information required for control from the energy-harvesting signal, while a periodic phase correction (PPC) technique is developed to resolve the mutual modulation between sensing and adjustment. On this basis, a large-step MPPT strategy is developed for the dual-parameter interface (energy extraction phase φ and voltage inversion ratio β), achieving rapid autonomous convergence. A prototype implementing the proposed method was fabricated and experimentally validated on two PEHs (PEH-1 and PEH-2). Experimental results show that both configurations successfully achieve sensorless fast auto-tuning, with 5.6-fold and 2.1-fold bandwidth improvements over traditional rectifiers for PEH-1 and PEH-2, respectively.**

***Index Terms*—Piezoelectric energy harvesting, adjustable-parameter interfaces, self-sensing, automatic control.**

I. Introduction

ENERGY harvesting has been widely studied as an effective method to power small-scale electronic devices such as monitoring sensors[1], fault detection [2], [3], smart devices [4], health care [5], [6], actuators [7]. In environments with abundant vibrations, piezoelectric energy harvesters (PEHs) have emerged as an especially promising solution for high power density for microscale applications [8]. However, when vibrations deviate from the resonant frequency or there is an impedance mismatch between the mechanical part and the electric part, the output power significantly decreases. To address this issue, researchers have proposed various adjustable-parameter interfaces (APIs) for frequency and impedance matching by introducing tunable interface parameters [9], [10], [11], [12], [13], [14]. The aforementioned studies fully demonstrate the significant role of APIs in maximizing energy harvesting over a broader bandwidth. Moreover, many aspects of the MPPT process have already been automated. For example, Morel et al. [15] proposed a fast-convergence self-adjusting synchronous electrical charge extraction (SECE) circuit with tunable short-circuit duration; Jiang et al. [16] developed a rectifier-less piezoelectric energy-harvesting interface with a sense-and-track MPPT; Moon et al. [17] presented a high-voltage power management integrated circuit using an efficient perturb and observe technique; and Yue et al. [18] introduced a bias-flip rectifier with duty-cycle-based MPPT. However, the above studies rely solely on peak detection or voltage comparison, providing limited sensing information that is insufficient to support complex multi-parameter interface auto-tuning. Then researchers conducted studies on multi-parameter automation. Gao et al. [19] proposed a prototyped self-sensing synchronous switch bidirectional energy conversion circuit (BBEC), Chen et al. [14] proposed a self-adaptive optimized synchronous electric charge extraction (SA-OSECE) circuit, and Decroix et al. [20] presented a two-load characterization method (TLCM) and a resistive short-circuit (RSC) interface. For most APIs, the tunable parameters are physically referenced to the mechanical oscillation cycle. Therefore, displacement-related timing information, especially the cycle phase and displacement extrema, serves as the natural feedback basis for interface tuning. For this reason, these multi-

This work was supported by the National Natural Science Foundation of China under Grants 52275574 and 52375131. (Corresponding author: Weiqun Liu).
Bo Qian, Jiahao Hu, and Weiqun Liu are with the Southwest Jiaotong University, Chengdu, 610031, China (e-mail: weiqunliu@home.swjtu.edu.cn).

Saikat Dutta is with University of Leeds, Leeds, LS2 9JT, UK (e-mail: S.Dutta@leeds.ac.uk).

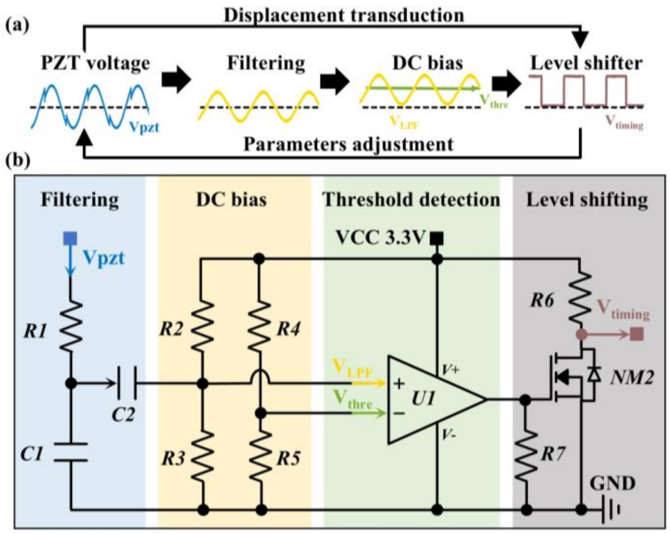

Fig. 1. (a) Schematic of displacement information recovery. (b) DIR module circuit topology.

parameter studies generally rely on external sensing devices, such as accelerometers, piezoelectric patches, or laser displacement sensors, to monitor vibration information in real time for control assistance, which limits the applicability of these API circuits outside laboratory settings.

In the absence of external sensor support, using the electrical signals generated by piezoelectric elements in response to mechanical excitation as the sensing signal source offers a good solution. Related studies [21], [22], [23], [24], [25] have shown that piezoelectric energy harvesters can support sensing or monitoring functions for environmental and motion-related information, thereby enabling self-powered sensing nodes. However, this energy-supplied sensing concept is different from the present work. Here, the intrinsic piezoelectric signal is not used as an environmental sensing output, but as the carrier of displacement-related timing information required for sensorless autonomous tuning of the adjustable-parameter interface.

Accordingly, we consider replacing external sensors with piezoelectric elements to obtain displacement-related feedback directly from the intrinsic electrical response. In this case, the distortion considered here is not ordinary measurement noise or generic waveform imperfection, but the self-induced modulation of the sensing signal caused by interface adjustment itself: the same piezoelectric voltage simultaneously carries the harvesting response and the displacement-related timing information, while the adjustment of (β, φ) perturbs that signal and distorts the feedback information, ultimately leading to a loss of control during the regulation process.

To address these challenges, this paper proposes a sensorless control scheme for APIs, capable of real-time analysis of the electrical signal characteristics from piezoelectric elements, providing instant feedback for dynamic adjustment of multi-parameter interfaces. Based on this scheme, we developed a large-step dual-loop MPPT strategy and designed a prototype, which was experimentally validated on two PEHs. To the best of our knowledge, this is the first multi-parameter interface

TABLE I
TUNING-RELATED VARIABLES & KEY SIGNAL DEFINITIONS

Symbol	Definition
φ/φ_x	Piezoelectric energy extraction phase, where x denotes a specified target phase
$\Delta\varphi/\Delta\varphi_n$	Amount of phase drift, where n denotes the cumulative drift over n cycles
β/β_i	Energy extraction inversion ratio, where i denotes a specified inversion ratio during the tuning process
$\beta_{opt\text{-}x}$	Optimal operating inversion ratio under a fixed phase φ_x
$(\beta_{init}, \varphi_{init})$	Initial operating parameters at the start of tuning
$(\beta_{opt}, \varphi_{opt})$	Global optimal operating point
V_{pzt}	Piezoelectric voltage signal
V_{LPF}	Bias signal after low-pass filtering
V_{thre}	Threshold signal
V_{timing}	Timing signal, a pulse square wave containing displacement-related timing information

control scheme that operates without reliance on external sensors or manual intervention. Experimental results demonstrate that both configurations successfully achieve fast sensorless self-tuning control, yielding bandwidth improvements of 5.6 times and 2.1 times over traditional rectifiers on PEH-1 and PEH-2, respectively.

The remainder of this paper is organized as follows. Section II introduces the principle of the sensorless control scheme. Section III presents the architecture of the designed interface. Section IV presents the experimental results and comparison. Finally, conclusions are drawn in Section V. For clarity, the definitions of all phase-related variables used throughout the paper are summarized in Table I at the beginning of Section II.

II. PRINCIPLE OF SENSORLESS CONTROL SCHEME

For effective API control, the controller must know where the PEH is within the mechanical oscillation cycle; therefore, displacement-related timing information is the key feedback for tuning the extraction phase and inversion ratio. In the absence of dedicated sensors, the inherent piezoelectric electrical signal becomes the exclusive carrier of mechanical vibration information. We developed a displacement information recovery (DIR) module that processes a low-pass filtered piezoelectric voltage (V_{LPF}) through threshold-based validation (V_{thre}) to extract displacement-related timing information (V_{timing}), as shown in Fig. 1(b). V_{timing} carries mechanical vibration information in its pulse-width, which enables direct processing by the microcontroller unit (MCU).

Evidently, as shown in Fig. 1(a), displacement information and adjustment behavior are strongly coupled. Variations in system parameters inevitably lead to variations in the piezoelectric signal, which in turn disrupts displacement information. Therefore, decoupling the V_{timing} and V_{pzt} signals is essential for achieving stable regulation.

To address this issue, we propose a periodic phase correction

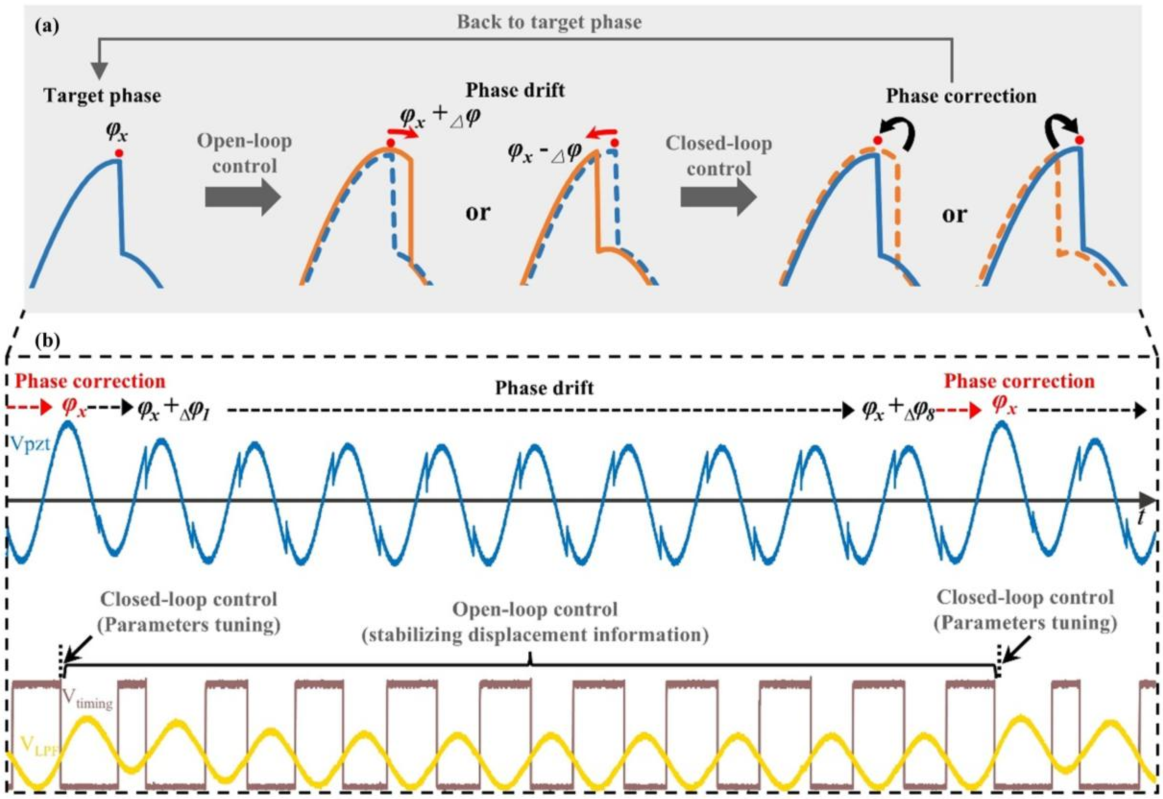

Fig. 2. (a) Operational logic of periodic phase correction approach. (b) Demonstration based on experimental waveforms.

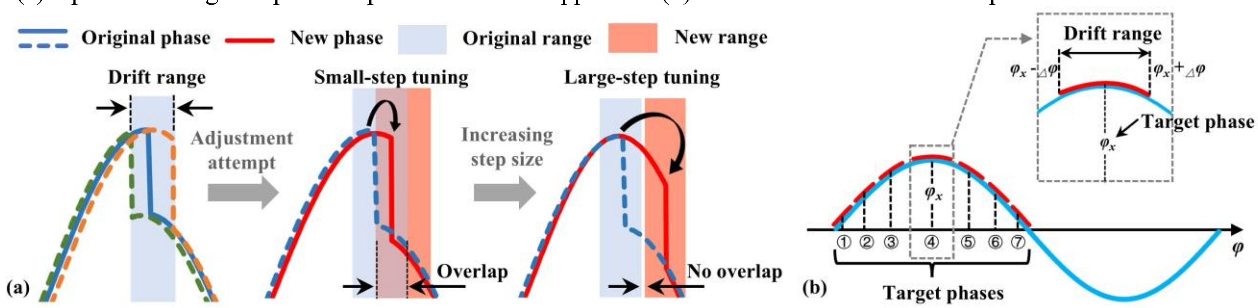

Fig. 3. (a) Principle of determining phase step size. (b) Target phases setting.

approach, as illustrated in Fig. 2, based on a hybrid control strategy that alternates between open-loop and closed-loop stages. During the open-loop phase, the energy extraction phase gradually drifts from the reference phase φ_x to $\varphi_x+\Delta\varphi_n$ over n operational cycles, allowing continuous power harvesting while tolerating controlled phase deviation. Once n cycles are completed, the system transitions to the closed-loop stage where the MCU's PWM peripheral actively adjusts the time delay to correct the phase back to φ_x, after which operation immediately reverts to the open-loop stage. This compound control strategy ensures that the phase remains within a predefined tolerance range, as illustrated in Fig. 2(a).

It should be noted, as shown in Fig. 2(b), that although closed-loop control effectively achieves phase correction, it also introduces disturbances due to mechanical vibration, leading to noticeable fluctuations in the filtered signal V_{LPF}. In contrast, open-loop control avoids these fluctuations but inevitably results in gradual phase drift, which accumulates into a deviation $\Delta\varphi_n$. The magnitude of $\Delta\varphi_n$ is closely related to the number of open-loop cycles n, while the direction of drift depends on the timing delay set during the open-loop stage. The value of n is selected by balancing the settling of the recovered timing signal and the allowable cumulative phase drift. Specifically, n should be large enough for V_{timing} to recover a stable period and amplitude after phase correction, while remaining small enough to keep the accumulated drift $\Delta\varphi_n$ within the prescribed correction band. Following this criterion, n=6-9 cycles is used in this prototype.

This compound control strategy ensures that the phase remains within a predefined tolerance range, as illustrated in Fig. 2(a). When the system operates at the target phase φ_x, the phase remains consistently confined within the interval $[\varphi_x-\Delta\varphi, \varphi_x+\Delta\varphi]$, thereby enabling stable and efficient regulation.

In this study, due to the presence of phase drift, the scale of phase adjustment becomes an important factor to consider. Although small-step phase adjustments are theoretically effective, they introduce non-negligible errors that hinder automatic control. In particular, overlapping phase drift intervals cause significant comparison errors, leading to failure of automatic optimization in practice. Therefore, we progressively increase the step size according to the procedure illustrated in Fig. 3(a) until the phase

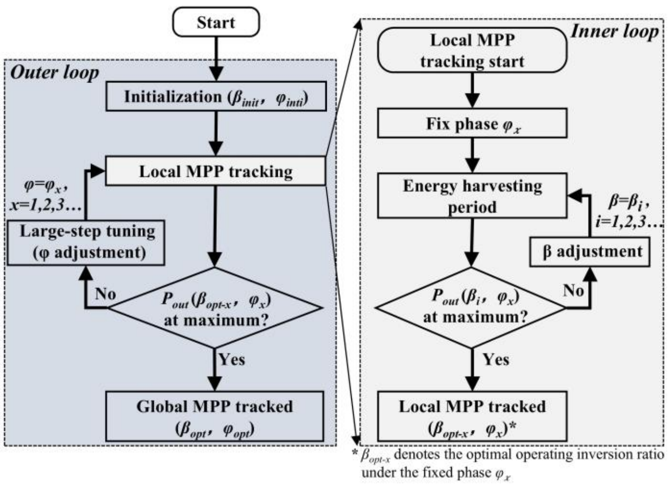

Fig. 4. Flow chart of proposed large-step MPPT.

drift ranges before and after adjustment become non-overlapping. By repeating the above process, the whole adjustable interval (π) is divided into a number of intervals, as shown in Fig. 3(b).

Before introducing the automated optimization process, it is necessary to clarify how the dual parameters β and φ influence the equivalent stiffness, damping, and output characteristics of the system in the FT-OSECE circuit adopted in this study, so that the regulation mechanism and purpose can be better understood. According to [13], the piezoelectric voltage V_{pzt} is non-sinusoidal, and can be expressed as

$$\begin{cases} V_{pzt} = \dfrac{\alpha x_m}{C_P}\left(\left(\cos\varphi - \dfrac{2\beta\cos\varphi}{1+\beta}\right) - \cos wt\right) & \varphi \le wt \le \pi + \varphi \\ V_{pzt} = \dfrac{\alpha x_m}{C_P}\left(-\left(\cos\varphi - \dfrac{2\beta\cos\varphi}{1+\beta}\right) - \cos wt\right) & \pi + \varphi \le wt \le 2\pi + \varphi \end{cases} \quad (1)$$

Here, α is the piezoelectric force factor, C_p is the capacitance of the piezoelectric element, and x_m denotes the displacement amplitude of the piezoelectric beam under harmonic excitation. In this sense, the present framework is mainly developed for harmonic or quasi-periodic excitation, where a stable cycle-level phase reference can be established for phase-controlled interface tuning. By performing Fourier decomposition, its fundamental frequency component V_1 can be obtained as

$$V_1 = \frac{\alpha}{C_p}(a_1 + jb_1)\tilde{x} \quad (2)$$

where $\tilde{x}$ is the complex expression of the displacement, and $a_1 = 1 + \frac{2}{\pi}\sin(2\varphi)\frac{1-\beta}{1+\beta}$ and $b_1 = \frac{4}{\pi}(\cos\varphi)^2\frac{1-\beta}{1+\beta}$.

Substituting these into the system's equations of motion $M\ddot{x} + D\dot{x} + K_0 x + \alpha V = M\gamma$, we obtain

$$-M\overline{w}^2\tilde{x} + \left(K_0 + a_1\frac{\alpha^2}{C_p}\right)\tilde{x} + j\left(D\overline{w} + b_1\frac{\alpha^2}{C_p}\right)\tilde{x} = M\overline{\gamma} \quad (3)$$

where K_0 is the short-circuit stiffness of the harvester, M and D are the equivalent mass and mechanical damping, γ is the base acceleration. Accordingly, the equivalent stiffness K_{eq} and electric damping D_e can be defined as

$$K_{eq} = K_0 + a_1\frac{\alpha^2}{C_p}, D_e = \frac{b_1}{\overline{w}}\frac{\alpha^2}{C_p} \quad (4)$$

It should be noted that Eqs. (2)-(4) describe the quasi-steady, cycle-averaged influence of (β, φ) on the equivalent stiffness and electrical damping, rather than the instantaneous behavior of every transient switching cycle. In the proposed PPC scheme, the open-loop phase drift is periodically corrected before accumulating excessively, so that the actual operating phase remains close to the condition assumed by the FT-OSECE model. Therefore, the residual mismatch mainly acts as a bounded implementation error in tuning accuracy, rather than a fundamental conflict with the Fourier-based formulation.

It can be observed that a_1 acts as the stiffness regulation factor, governing the magnitude of the equivalent stiffness. Correspondingly, b_1 serves as the damping regulation factor, modulating the electrical damping of the system. Therefore, maximum output power can be achieved by tuning a_1 to modify K_{eq}, thereby aligning the equivalent resonant frequency with the excitation frequency, and by tuning b_1 to regulate D_e, so that the electrical damping equals the mechanical damping, which realizes maximum power transfer. Second, the adjustment of b_1 also enables bandwidth extension, since increasing the effective electrical damping broadens the operational frequency range of the harvester.

To realize the above objectives of tuning equivalent stiffness and electrical damping, we propose a large-step MPPT strategy that employs a dual-loop regulation scheme to achieve optimal tracking of (β, φ), as shown in Fig. 4. The procedure operates as follows: the inner loop adjusts β_i under a fixed phase φ_x , and measures the corresponding output power P_{out} (β_i, φ_x). This process continues until the power ceases to increase, at which point the corresponding operating condition is recorded as the local MPP, denoted by ($\beta_{opt\text{-}x}$, φ_x). Meanwhile, the outer loop performs a large-step adjustment of the phase φ_x, and compares the output power across different local MPPs. When no further increase in power is observed, the corresponding parameters are identified as the global MPP, denoted by (β_{opt}, φ_{opt}).

III. Designed Interface Architecture

To verify the feasibility of the proposed sensorless control scheme, we developed an automated API based on the frequency-tuning optimized synchronous electric charge extraction (FT-OSECE) interface [13], which incorporates two key parameters—the piezoelectric energy extraction phase (φ) and the inversion ratio (β)—to achieve frequency and impedance matching. Figure 5 illustrates the architecture of the interface, which includes a low-power microcontroller unit (LPMCU), energy harvesting channels (EHCs, including OSECE-based channel and half-bridge channel), an energy management unit (EMU), a DIR unit, a wireless unit, an ADC signal conditioner, and a low-voltage selector (LVS) [26].

The operational principle of the system is as follows: When the system is subjected to vibration excitation, the half-bridge channel automatically starts harvesting energy and stores it in the capacitor-based storage path (the front-end capacitor C_{sto} and the LTC3588-based EMU). Once sufficient energy is accumulated, the harvesting channel switches to the OSECE-based channel. Concurrently, the DIR unit and LPMCU are activated. The DIR unit processes the piezoelectric signal V_{pzt} through filtering, biasing, and level shifting to generate the timing signal V_{timing}. The LPMCU analyzes the vibration state

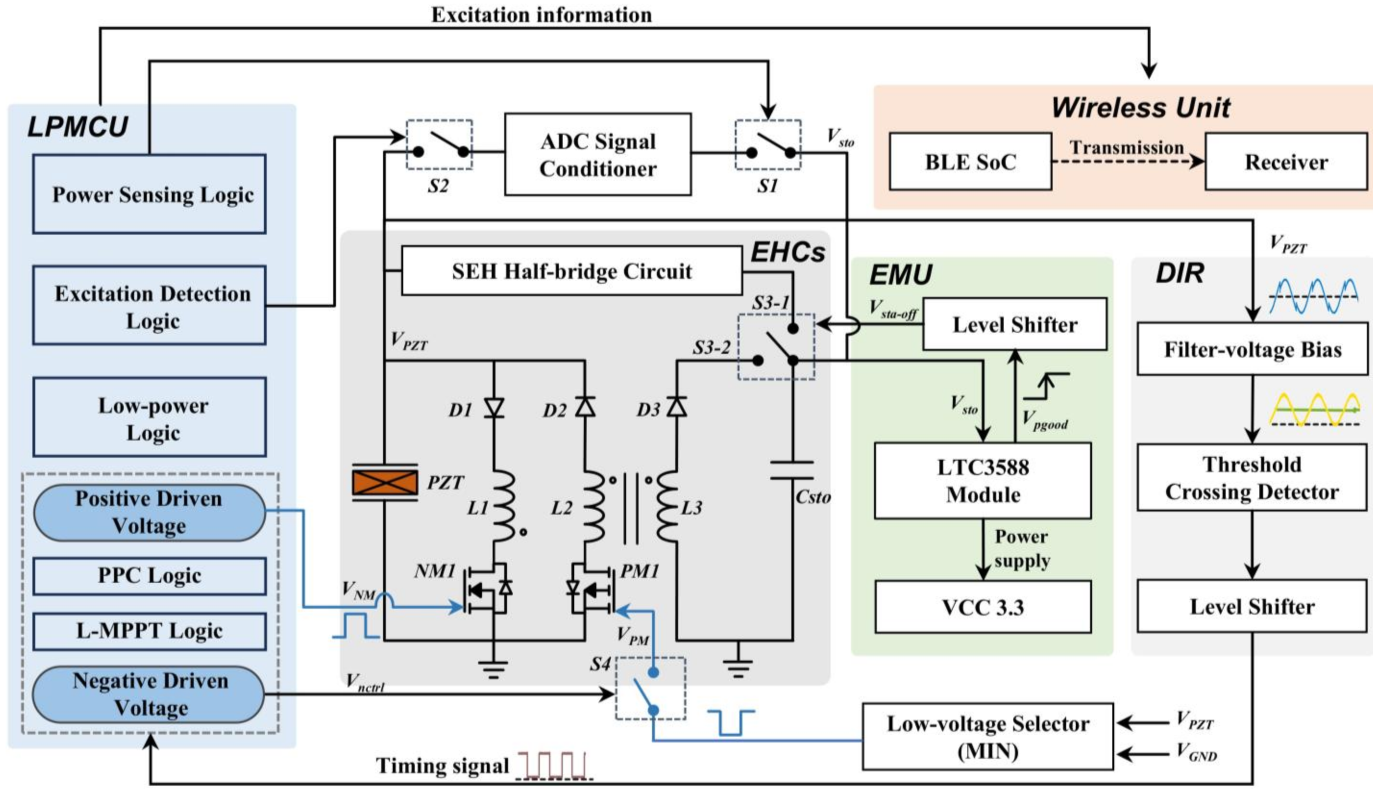

Fig. 5. Architecture of designed automated API.

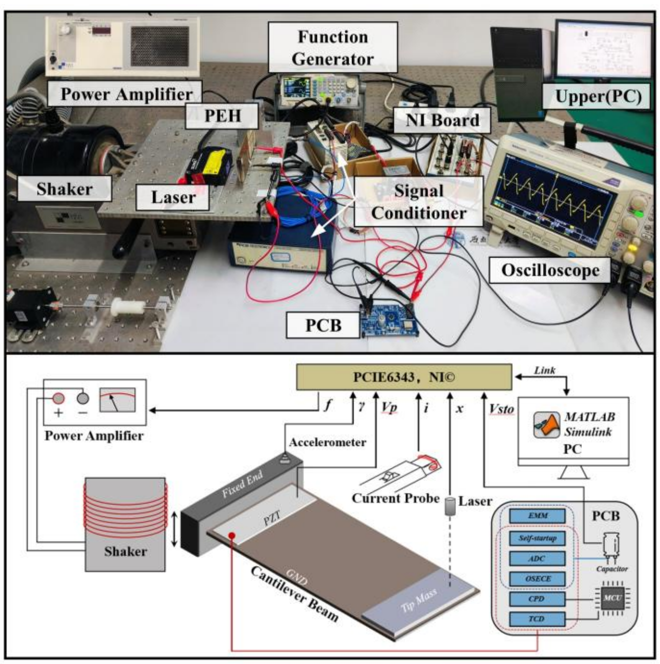

Fig. 6. Experimental platform and schematic diagram.

of the PEH in real time via the V_{timing} signal and, based on the designed large-step MPPT strategy, controls the turn-on timing and duration of switches NM1 and PM2. During this process, the LVS assists in enabling the PM2 switch, and ADC signal conditioner acquires changes in energy storage to support the MPPT strategy.

In this architecture, the DIR module provides sensorless phase-reference extraction, the PPC technique provides phase-reference stabilization, and the large-step MPPT strategy provides automatic optimal-parameter search. These three functions are indispensable and jointly support the overall sensorless autonomous tuning performance demonstrated in this work.

It is worth noting a small but important design detail of the DIR module: a high-impedance front-end divider attenuates the open-circuit piezoelectric voltage, such that the peak-to-peak voltage of V_{LPF} remains below 1.6 V. Specifically, the open-circuit piezoelectric voltage V_{pzt} is attenuated by a 10 MΩ / 200 kΩ divider, limiting the attenuated signal to approximately ±0.78 V under the tested conditions; therefore, V_{bias}=0.9 V was selected to keep the biased V_{LPF} safely within the MCU input range. A resistive bias network (R2-R5) centers the filtered signal at V_{bias} =0.9 V, with the comparator threshold Vthre aligned to this bias voltage. Although V_{bias} and V_{thre} are both set to 0.9 V, they have different roles: V_{bias} provides the DC offset for the attenuated piezoelectric signal, whereas V_{thre} defines the virtual zero-crossing level for the comparator. As a result, the comparator triggers when the filtered signal crosses the preset threshold (aligned with V_{bias}), generating a robust timing pulse, V_{timing}.

In addition, our design incorporates application-oriented vibration sensing and wireless transmission capabilities. Upon completing optimal parameters (β_{opt}, φ_{opt}) tracking, the system initiates comprehensive vibration information acquisition from the PEH and transmits the information wirelessly to the terminal.

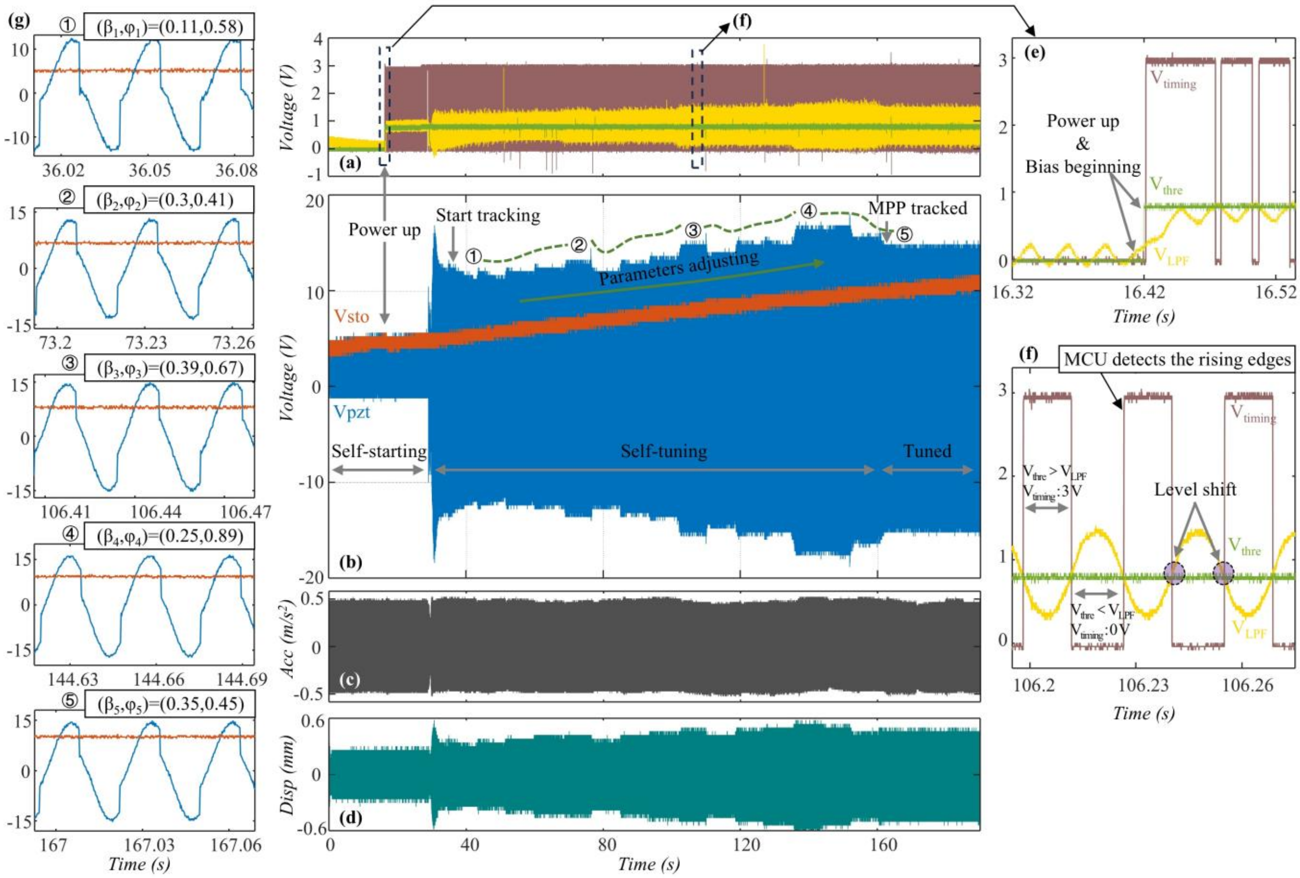

Fig. 7. Experimental waveforms of the L-MPPT method. (a) V_{LPF}, V_{thre} and V_{timing}. (b) V_{pzt} and V_{sto}. (c) Acceleration. (d) Displacement. (e) Zoomed view of power-up instant. (f) Waveform of DIR. (g) Zoomed views of different stages.

TABLE II
CHARACTERISTICS OF PEHS & COMPONENT LIST

Symbol	Definition / Value	PEH-1	PEH-2
C_p	PZT Capacitance	220 nF	212 nF
α	Piezoelectric Coefficients	4e-3	16e-3
Q_m	Mechanical Quality Factor	270	100
Q_I	Circuit Quality Factor	3	3
k^2_m	Coupling coefficient	0.04	0.028
f_r	Resonant Frequency	35.8 Hz	86.0 Hz
M	Terminal Mass	22.5g	98.5g
$R_{1,6,7}$	10 MΩ	-	-
R_2	5.6 MΩ	-	-
R_3	2.4 MΩ	-	-
R_4	3.9 MΩ	-	-
R_5	1.5 MΩ	-	-
NM_1	Si2309	-	-
NM_2	BSS138PW	-	-
PM_1	Si2392	-	-
L_{1-3}	MSD1278T-105	-	-
D_{1-3}	NSR02100HT1G	-	-
C_1	0.3 nF	-	-
C_2	10 nF	-	-
U_1	ADA4505-1ARJZ-R7	-	-

IV. EXPERIMENTAL VALIDATION

The fabricated prototypes, denoted as PEH-1 and PEH-2, are shown in Fig. 8(a). Both PEHs use PZT-4 patches (Jiayida©) as energy harvesting elements: PEH-1 on a beryllium-copper substrate (137×62×1.2 mm³) with 0.2-mm-thick patches (7200 mm^2), and PEH-2 on a steel substrate (92×65×2 mm³) with 0.4-mm-thick patches (7200 mm^2). An integrated four-layer modular printed circuit board (PCB) was specially fabricated based on the proposed interface, as shown in Fig. 8(a). The layout of each module is detailed in the silkscreen. The PEHs are connected to the V_{pzt} and *GND* pins on PCB, and fixed to the base of a shaker (The Modal Shop©, 2075E-HT). Fig. 6 illustrates the entire experimental platform and its schematic. The closed-loop system consists of the shaker, power amplifier, computer software (MATLAB©), and data acquisition card (NI©, PCIe-6343), which provides excitation with constant acceleration. An accelerometer and a laser sensor (SUNX©, HL-C203BE) are employed to measure acceleration and displacement. A current probe (Tektronix©, TCPA) is used to measure the system operating current, and an oscilloscope (Tektronix, MDO3024) is used to measure and observe the signals.

Fig. 7(b) demonstrates the three-stage adjustment process of the proposed interface under controlled excitation conditions (0.05 g acceleration, 36.8 Hz frequency). Initially, when the system is in an energy-deficient state, it operates in the cold-

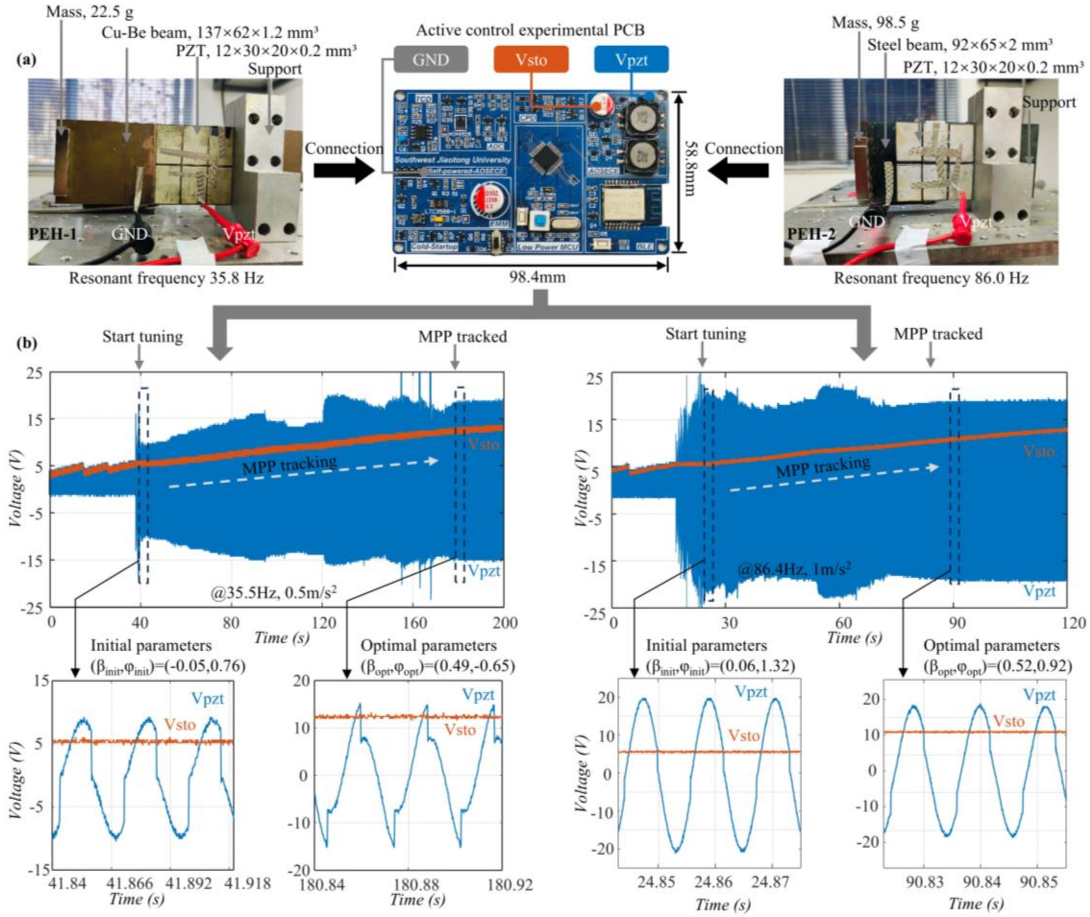

Fig. 8. (a) Fabricated prototype (PCB) and PEHs (PEH-1 and PEH-2). (b) Waveforms and results of self-adjustment experiments.

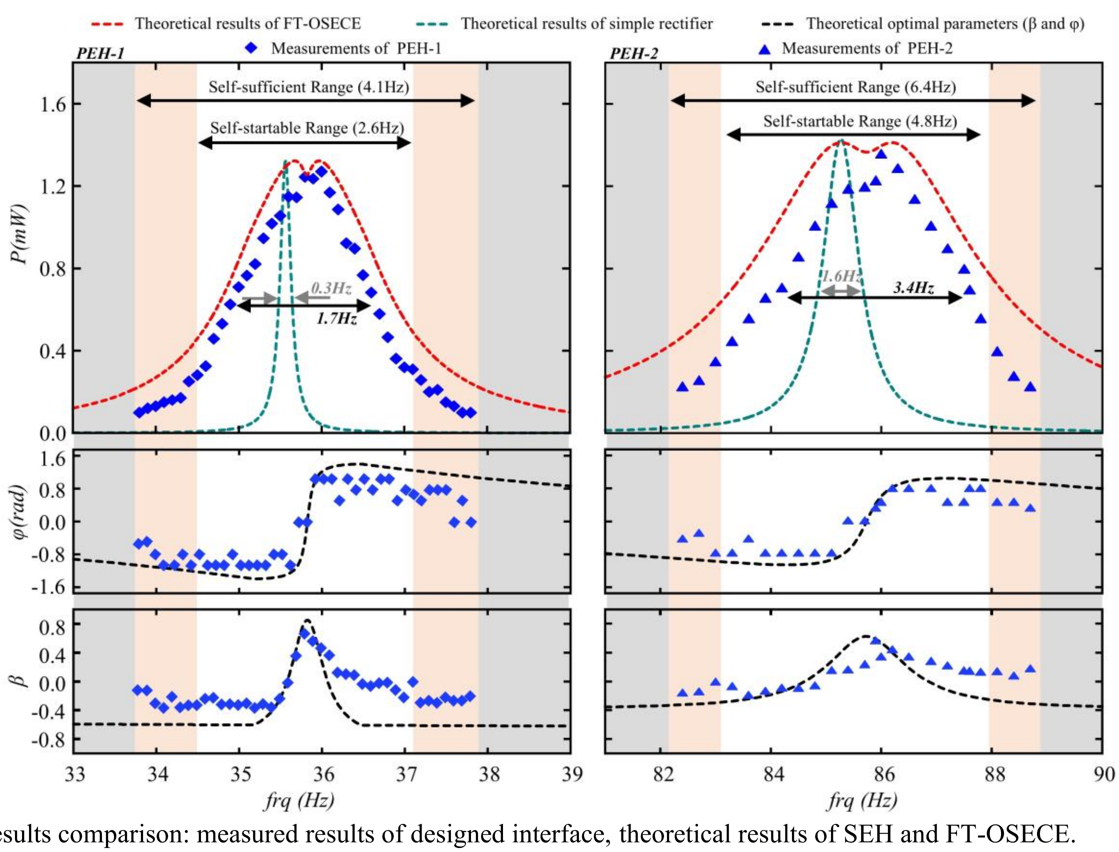

Fig. 9. Results comparison: measured results of designed interface, theoretical results of SEH and FT-OSECE.

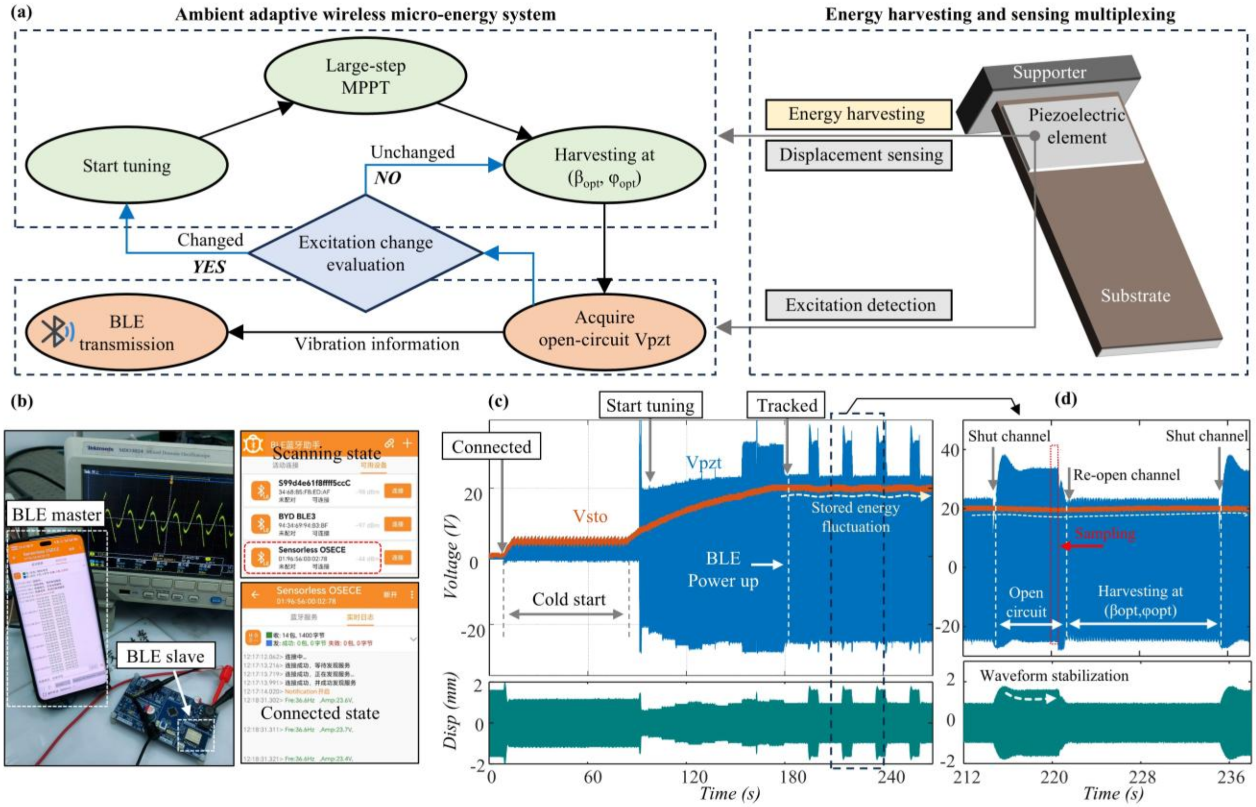

Fig. 10. Application experiment. (a) State machine of ambient adaptive wireless micro-energy systems and schematic diagram of sensorless generator. (b) Demonstration of BLE application. (c) Waveforms of the micro-system. (d) Zoomed waveforms of ambient detection phase.

TABLE III
DIR MODULE ERROR EVALUATION

Frequency [Hz]	34.6	35.1	35.6	36.1	36.6
e_T [%]	0.0147	0.0052	0.0083	0.1913	0.2418

*: e_T=|T_{timing}-T_{disp}|/ T_{disp}×100%, where T_{timing} is the period extracted from the rising edges of V_{timing}, and T_{disp} is the displacement period obtained from the laser displacement sensor

start stage. The SEH half-bridge circuit spontaneously extracts vibration energy into the storage capacitor C_{sto}, and the EMU transfers energy from C_{sto} to the regulated supply capacitor. Once the 3.3 V threshold is reached, the LTC3588 activates the LPMCU and DIR units, as shown in Fig. 7(e), thereby triggering the transition from the half-bridge channel to the adjustable OSECE-based channel. The self-tuning stage then starts, during which the large-step MPPT algorithm rapidly converges to the optimal parameters (β_{opt}, φ_{opt}), after which the system enters the optimal-operation stage. Thus, Fig. 7 provides a complete time-domain view of the cold-start, self-tuning, and optimal-operation stages.

Fig. 7(b) labels the PEH states at five different parameters during the self-regulation process, and the five states are zoomed in Fig. 7(g). In the initial state (①), the parameters (β_1, φ_1) are set to (0.11, 0.58) and V_{pzt} amplitude is 12 V; in the final optimized state (⑤), the parameters (β_5, φ_5) are set to (0.35, 0.45), with a V_{pzt} amplitude of 15 V. Fig. 7(c) and (d) show the variations in acceleration and displacement, while Fig. 7(f) displays the real-time waveforms of V_{LPF}, V_{thre}, and V_{timing}.

This study conducted two sets of PEH experiments, with the characteristic parameters of the PEHs listed in Table II. The two PEHs provide representative single-mode cases with different resonant frequencies and electromechanical parameters, allowing us to examine whether the same DIR-PPC-MPPT framework can be applied without redesigning the core control principle. Fig. 8(b) summarizes the autonomous self-adjustment results for both PEHs. For PEH-1, under 35.5 Hz and 0.5 m/s² excitation, the operating point is automatically adjusted from the initial state (β_{init}, φ_{init}) = (-0.05, 0.76) to the final state (β_{opt}, φ_{opt}) = (0.49, -0.65). A similar autonomous tuning process is also observed for PEH-2 under 86.4 Hz excitation. Fig. 9 further shows that the proposed interface broadens the effective harvesting bandwidth for both PEHs within the considered harmonic-excitation scope.

To verify repeatability, the key frequencies determining the -3 dB bandwidth and the peak power were measured 10 times under identical excitation and loading conditions, and the resulting bandwidth and peak-power variations remained within about 3%. In addition, a continuous PPC test lasting about 2 h confirmed that the extraction phase remained bounded around the target value without observable cumulative drift, supporting the long-term robustness of the DIR-PPC control process. The DIR timing accuracy was evaluated by comparing V_{timing} with the laser-measured displacement at five frequencies. The filtering-induced phase error is nearly constant and does not affect the final optimization result, so the possible DIR phase jitter was quantified using the normalized period mismatch e_T. As shown

TABLE IV
COMPARISON WITH STATE-OF-THE-ART SOLUTION

References	[14]	[15]	[18]	[20]	[27]	[28]	**This work**
Harvesting technique	SA-OSECE	Shorted SECE	SSHI	RSC	PS-SECE	TCAS	**FT-OSECE**
Tuning parameters (Nb of tuning)	voltage reversal ratio β, extraction phase φ (2)	SC duration $\Delta\Phi$ (1)	cut-off duty cycle (1)	SC duration $\Delta\Phi$, Load R_{RSC} (2)	extraction phase φ (1)	amplitude V_C, phase θ_C (2)	**voltage reversal ratio β, extraction phase φ (2)**
Technology	MCU	IC (0.6 μm)	IC (0.18 μm)	MCU	IC (0.6 μm)	MCU	**MCU**
MPPT strategy	P&O	P&O	DCB	TLCM	P&O	O&O	**P&O**
Tracking efficiency	92%*	94%	98%	-	94%	-	**84%**
FoM(a) (convergence)	1.2%*	21.3%	-	65.7%*	3.8%	-	**5.39%**
FoM(b) (bandwidth)	1081%*	368%	-	734%*	446%	-	**1133%**
Power consumption [μW]	63.71	0.03	0.307	21.5~28.5	0.6	-	**<70**
Sensing method	vibration detection	peak detection	voltage comparison	vibration detection	peak detection	vibration detection	**vibration detection**
Additional sensors	piezoelectric patches	none	none	accelerometer	none	accelerometer	**none**

*: Calculated or estimated from the paper -: Not reported

(a) FoM (convergence) = Q_m / (τ f_{res}), where τ is the convergence time of the MPPT algorithm [15]

(b) FoM (bandwidth) = bandwidth of the output power over the natural bandwidth of the transducer (f_{res} / Q_m) [15]

in Table III, e_T remained below 0.5%, indicating that the jitter has little influence on phase-controlled tuning.

The higher operating frequency of PEH-2 (about 2.54 times that of PEH-1) increases the interface's wake-up rate and, consequently, its energy consumption. Under off-resonance excitation, the harvested energy is reduced, whereas the high-frequency MCU operation remains almost unchanged and thus dominates the output power budget. Meanwhile, the reduced vibration amplitude flattens the power-versus-parameter response, so that the power increment produced by adjacent (β, φ) adjustments becomes much smaller than that near resonance. In this low-output regime, the energy variation between successive MPPT steps becomes very small and is easily buried in measurement noise and random fluctuations, so that the incremental changes used by the MPPT algorithm are no longer reliably distinguishable. As a result, a noticeable reduction in tuning accuracy is observed for both PEHs under off-resonance conditions.

From a system-level perspective, the practical benefit of the proposed interface should be evaluated in terms of net power after subtracting the circuit overhead, i.e., $P_{net} = P_{harvested} - P_{overhead}$. Under the representative PEH-1 operating condition, $P_{harvested} \approx$ 1.22 mW and the measured total interface overhead is about 69.3 μW, yielding a positive net power of about 1.15 mW and a post-harvest energy utilization efficiency of about 94.3%. If only the added MCU and DIR overhead is considered, the corresponding utilization efficiency is about 95.7%. Therefore, although the added sensing and control circuits consume power, their overhead remains only a small fraction of the harvested energy. Moreover, the broadened bandwidth in Fig. 9 should be interpreted together with the self-sufficient operating region: within the experimentally identified self-sufficient range, the harvested power remains higher than the circuit overhead, so the system is net-energy-positive; outside this range, positive self-powered operation is not claimed.

Additionally, experiments on self-starting and external power supply startup were conducted to explore the performance limits. The self-starting region (white) indicates that the system can start with zero stored energy, while the self-sufficient region (orange) indicates that the system can continue operating after startup. The boundary values were determined experimentally by gradually reducing the available harvested power and checking whether the prototype could still autonomously complete cold start, activate the control circuitry, and maintain stable self-adjusted operation after startup. Under these criteria, the corresponding boundary output powers are 0.2 mW for PEH-1 and 0.32 mW for PEH-2. These values are practical reference thresholds for the present prototype rather than universal theoretical limits, since they depend on the harvester characteristics, excitation conditions, and circuit power consumption.

To assess the practical applicability of the proposed hardware-control co-design, we developed an ambient adaptive wireless micro-energy system (WMS) based on Bluetooth low energy (BLE, ADA14580), as shown in Fig. 10(a). The basic logic of the system is that, after completing the self-starting and self-tuning stages, the system will operate at the optimal point. Then, every 12 seconds, all energy harvesting channels are briefly disabled to acquire the open-circuit piezoelectric signal and calculate the excitation frequency (accuracy: 0.1 Hz) and piezoelectric amplitude (accuracy: 0.1 V). When a significant change in excitation is detected, the system will re-initiate the search for the optimal operating point. Figures 10(b) and (c) show the wireless micro-energy system operating from zero energy storage, functioning as a BLE slave, collecting and transmitting excitation information, with a smartphone receiving the information. For this application-oriented prototype, the measured cold-start latency of PEH-1 under the representative tested excitation of 0.5 m/s² is about 90 s, defined as the time from the onset of vibration with zero initial stored energy to the establishment of the regulated 3.3 V output and MCU activation.

Table IV compares the proposed sensorless automatic parameter tuning scheme with current advanced automatic API control technologies. For a clearer comparison, these methods can be roughly divided into three categories: sensorless single-parameter methods [15], [18], [27], multi-parameter methods assisted by external vibration sensing or model-based characterization [14], [20], [28], and the proposed sensorless dual-parameter scheme. Existing sensorless methods [15], [18], [27] are limited by the low information content of self-sensed signals, and thus can only support single-parameter automatic tuning. Meanwhile, current multi-parameter automatic control schemes [14], [20], [28] have not yet eliminated the reliance on vibration sensors or additional characterization, due to the inherent complexity of multi-parameter interface control.

In terms of control accuracy, the proposed method achieves a tracking efficiency of 84%, which is lower than that of some sensor-assisted or single-parameter methods. For example, the homologous dual-parameter work [14] reports a tracking efficiency of 92%. This moderate loss in tracking accuracy mainly reflects the challenge of realizing dual-parameter autonomous tuning without external vibration sensors. Nevertheless, the proposed method still enables fully sensorless optimization of both β and φ, which is the main distinction from prior sensor-assisted dual-parameter approaches.

In terms of convergence and bandwidth improvement, the proposed large-step P&O strategy achieves a convergence FoM of 5.39%, which is about 4.5 times higher than the estimated 1.2% of [14]. More importantly, the bandwidth FoM reaches 1133%, which is higher than those of [15] (368%), [20] (734%), and [27] (446%), and slightly higher than the homologous dual-parameter work [14] (1081%). Therefore, although the proposed method sacrifices a moderate amount of tracking accuracy, it provides a competitive bandwidth enhancement while eliminating additional vibration sensors. This comparison indicates that the proposed scheme offers a practical trade-off between control accuracy, convergence speed, bandwidth improvement, and sensorless autonomy.

V. Conclusion

The practical implementation of APIs has long been constrained by the absence of self-sensing capabilities, where existing sensing-enabled harvesters fail to autonomously adjust multi-parameter interfaces. However, in the absence of additional sensors, two critical challenges must be resolved: (1) accurate recovery of mechanical vibration information from inherent electrical signals, and (2) effective decoupling between parameter adjustment behaviors and dynamic responses. To address these challenges and enable autonomous adjustment in APIs, this paper proposes a sensorless control scheme that achieves real-time recovery of displacement-related information from piezoelectric signals, along with PPC technique to decouple displacement information and adjustment behavior. In order to validate the proposed scheme, we developed a large-step MPPT strategy and implemented a functional prototype interface for experimental verification. Experimental results show that both configurations successfully realize sensorless fast auto-tuning, with 5.6-fold and 2.1-fold bandwidth improvements over traditional rectifiers for PEH-1 and PEH-2, respectively.

The proposed method is mainly intended for compact self-powered PEH systems using APIs under harmonic or quasi-periodic excitation, especially in remote or unattended scenarios where the vibration contains a stable dominant frequency or several discrete periodic components, such as rotating machinery in gas pipeline stations, offshore platforms, and mining or tunnel ventilation systems; meanwhile, its tuning accuracy degrades under off-resonance low-gradient conditions, and the startup threshold and net-energy performance remain implementation-dependent.

References

[1] X. Tang, X. Wang, R. Cattley, F. Gu, and A. D. Ball, "Energy Harvesting Technologies for Achieving Self-Powered Wireless Sensor Networks in Machine Condition Monitoring: A Review," Sensors, vol. 18, no. 12, p. 4113, Nov. 2018.

[2] W. Li et al., "Vibrational Triboelectric Nanogenerator-Based Multinode Self-Powered Sensor Network for Machine Fault Detection," IEEE/ASME Trans. Mechatron., vol. 25, no. 5, pp. 2188–2196, Oct. 2020.

[3] H. J. Jung, A. T. Eshghi, and S. Lee, "Structural Failure Detection Using Wireless Transmission Rate from Piezoelectric Energy Harvesters," IEEE/ASME Trans. Mechatron., vol. 26, no. 4, pp. 1708–1718, Aug. 2021.

[4] M. Cai and W.-H. Liao, "Design, Modeling, and Experiments of Electromagnetic Energy Harvester Embedded in Smart Watch and Wristband as Power Source," IEEE/ASME Trans. Mechatron., vol. 26, no. 4, pp. 2104–2114, Aug. 2021.

[5] S. Almouahed, M. Gouriou, C. Hamitouche, E. Stindel, and C. Roux, "The Use of Piezoceramics as Electrical Energy Harvesters Within Instrumented Knee Implant During Walking," IEEE/ASME Trans. Mechatron., vol. 16, no. 5, pp. 799–807, Oct. 2011.

[6] M. Safaei, R. M. Meneghini, and S. R. Anton, "Energy Harvesting and Sensing with Embedded Piezoelectric Ceramics in Knee Implants," IEEE/ASME Trans. Mechatron., vol. 23, no. 2, pp. 864–874, Apr. 2018.

[7] F. Khoshnoud et al., "Energy Regeneration from Suspension Dynamic Modes and Self-Powered Actuation," IEEE/ASME Trans. Mechatron., vol. 20, no. 5, pp. 2513–2524, Oct. 2015.

[8] S. Sharma, R. Kiran, P. Azad, and R. Vaish, "A review of piezoelectric energy harvesting tiles: Available designs and future perspective," Energy Conversion and Management, vol. 254, p. 115272, Feb. 2022.

[9] A. Richter, A. Strobel, N. Joram, F. Ellinger, L. Gopfert, and R. Marg, "Tunable interface for piezoelectric energy harvesting," in 2014 IEEE 11th International Multi-Conference on Systems, Signals & Devices (SSD14), Castelldefels-Barcelona, Spain: IEEE, Feb. 2014, pp. 1–5.

[10] E. Lefeuvre, A. Badel, A. Brenes, S. Seok, and C.-S. Yoo, "Power and frequency bandwidth improvement of piezoelectric energy harvesting devices using phase-shifted synchronous electric charge extraction interface circuit," Journal of Intelligent Material Systems and Structures, vol. 28, no. 20, pp. 2988–2995, Dec. 2017.

[11] A. Brenes et al., "Large-bandwidth piezoelectric energy harvesting with frequency-tuning synchronized electric charge extraction," Sensors and Actuators A: Physical, vol. 302, p. 111759, Feb. 2020.

[12] Y. Wu, A. Badel, F. Formosa, W. Liu, and A. Agbossou, "Self-powered optimized synchronous electric charge extraction circuit for piezoelectric energy harvesting," Journal of Intelligent Material Systems and Structures, vol. 25, no. 17, pp. 2165–2176, Nov. 2014.

[13] W. Tian, Z. Zhao, W. Liu, Q. Zhu, Z. Zhang, and Y. Yuan, "Analysis on the power and bandwidth improvement of a frequency-tuning optimized SECE circuit," Sensors and Actuators A: Physical, vol. 332, p. 113110, Dec. 2021.

[14] Chen, K., Zhuo, J., Liu, W., Huang, Y., Hua, C., Zhu, Q., & Yuan, Y. (2024). Self-sensed, self-adapted and self-powered piezoelectric generator architecture by synchronous circuits of autonomous parameter tuning. Energy Conversion and Management, 300, 117919.

[15] A. Morel et al., "Fast-Convergence Self-Adjusting SECE Circuit With Tunable Short-Circuit Duration Exhibiting 368% Bandwidth Improvement," IEEE Solid-State Circuits Lett., vol. 3, pp. 222–225, 2020.

[16] S. Jiang, X. Yue, Y. Ma, C. Wang, and S. Du, "A Rectifier-Less Piezoelectric Energy-Harvesting Interface with a Sense & Track MPPT Achieving Single-Cycle Convergence and 568% Shock Power Improvement," in 2025 IEEE International Solid-State Circuits Conference (ISSCC), San Francisco, CA, USA: IEEE, Feb. 2025, pp. 522–524.

[17] S.-Y. Moon, A. Shafique, S. C. Chandrarathna, and J.-W. Lee, "A High-Voltage PMIC Using an Efficient Perturb and Observe Technique for Energy Harvesting of Triboelectric Nanogenerators," IEEE Trans. Power Electron., vol. 40, no. 2, pp. 3225–3239, Feb. 2025.

[18] X. Yue, S. Javvaji, Z. Tang, K. A. A. Makinwa, and S. Du, "A Bias-Flip Rectifier With Duty-Cycle-Based MPPT for Piezoelectric Energy Harvesting," IEEE J. Solid-State Circuits, vol. 59, no. 6, pp. 1771–1781, Jun. 2024.

[19] L. Gao, L. Teng, H. Wang, Y. Liu, M. Fu, and J. Liang, "A Self-Sensing Synchronous Switch Circuit for Bidirectional Piezoelectric Energy Conversion," IEEE Trans. Ind. Electron., vol. 71, no. 9, pp. 11592–11601, Sep. 2024.

[20] N. Decroix, P. Gasnier, A. Morel, D. Gibus, and A. Badel, "A Low-Power MCU-Based MPPT Architecture With a Fast Impedance Measurement for Broadband Piezoelectric Energy Harvesting," IEEE Trans. Power Electron., vol. 39, no. 11, pp. 14815–14826, Nov. 2024.

[21] L. Qin et al., "A hybrid triboelectric-piezoelectric smart squirrel cage with self-sensing and self-powering capabilities," Nano Energy, vol. 124, p. 109506, Jun. 2024.

[22] L. L. Ruiz et al., "Piezoelectric-Based Respiratory Monitoring: Towards Self-Powered Implantables for the Airways," in 2021 IEEE 17th International Conference on Wearable and Implantable Body Sensor Networks (BSN), Athens, Greece: IEEE, Jul. 2021, pp. 1–5.

[23] X. Wang, H. Xia, Y. Xia, Y. Ye, G. Shi, and X. Chai, "Energy Harvesting and Acceleration Measuring Based on Time-Division Multiplexing Operation of a Single Piezoelectric Transducer," IEEE Trans. Power Electron., vol. 38, no. 5, pp. 5644–5648, May 2023.

[24] J. B. Liseli, J. Agnus, P. Lutz, and M. Rakotondrabe, "An Overview of Piezoelectric Self-Sensing Actuation for Nanopositioning Applications: Electrical Circuits, Displacement, and Force Estimation," IEEE Trans. Instrum. Meas., vol. 69, no. 1, pp. 2–14, Jan. 2020.

[25] Z. J. Chew, T. Ruan, M. Zhu, M. Bafleur, and J.-M. Dilhac, "Single Piezoelectric Transducer as Strain Sensor and Energy Harvester Using Time-Multiplexing Operation," IEEE Trans. Ind. Electron., vol. 64, no. 12, pp. 9646–9656, Dec. 2017.

[26] A. Shareef, W. L. Goh, S. Narasimalu, and Y. Gao, "A Rectifier-Less AC–DC Interface Circuit for Ambient Energy Harvesting from Low-Voltage Piezoelectric Transducer Array," IEEE Trans. Power Electron., vol. 34, no. 2, Art. no. 2, Feb. 2019.

[27] A. Morel et al., "32.2 Self-Tunable Phase-Shifted SECE Piezoelectric Energy-Harvesting IC with a 30nW MPPT Achieving 446% Energy-Bandwidth Improvement and 94% Efficiency," in 2020 IEEE International Solid- State Circuits Conference - (ISSCC), San Francisco, CA, USA: IEEE, Feb. 2020, pp. 488–490.

[28] L. Costanzo, A. Lo Schiavo, and M. Vitelli, "Active Interface for Piezoelectric Harvesters Based on Multi-Variable Maximum Power Point Tracking," IEEE Trans. Circuits Syst. I, vol. 67, no. 7, pp. 2503–2515, Jul. 2020.

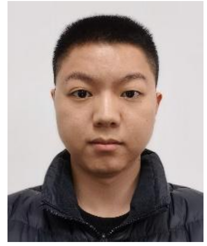

Bo Qian received the B.S. degree in vehicle engineering from the Xihua University, Chengdu, China, in 2022. He is currently working toward the Ph.D. degree in mechanical design and theory with Southwest Jiaotong University, China.

His research interests include energy harvesting, vibration control, IoT devices and mechatronics.

Jiahao Hu received the B.S. degree in energy and power engineering in 2021 from the School of Mechanical Engineering, Southwest Jiaotong University, Chengdu, China, where he is currently working toward the Ph.D. degree in vehicle engineering.

His research interests include energy harvesting, fuel cell durability, and health assessment under vibration conditions.

Saikat Dutta received Ph.D. degree in Mechanical Engineering researching vibration isolation using Magneto-rheological dampers from Indian Institute of Technology Kharagpur, India, in 2015. He is an Assistant Professor with the School of Mechanical Engineering, University of Leeds, U.K. His current research work is concentrated on nonlinear vibration analysis, vehicle dynamics, control and fault detection, particularly focusing on automotive and railway applications. Dr Dutta is a Chartered Engineer and a Member of the Institution of Mechanical Engineers.

Weiqun Liu (Member, IEEE) was born in Hengyang, China, in 1983. He received the B.S. and M.S. degrees in mechanical engineering from the University of Science and Technology of China, Hefei, China, in 2005 and 2008, respectively, and the Ph.D. degree in engineering science from the Université de Grenoble Alpes, Grenoble, France, in 2015.

He is currently a Professor with the Department of Mechanical Engineering, Southwest Jiaotong University, China. His research interests include energy harvesting, smart material systems and structures, nonlinear dynamics, and battery management system.